

Article

Not peer-reviewed version

---

# Extended Short-Wave Infrared T2SL Detector Based on AlAsSb/GaSb Barrier Optimization

---

[Jing Yu](#), [Yuegang Fu](#), [Lidan Lu](#), Weiqiang Chen, [Jianzhen Ou](#)<sup>\*</sup>, [Liangjing Zhu](#)<sup>\*</sup>

Posted Date: 4 March 2025

doi: 10.20944/preprints202503.0202.v1

Keywords: eSWIR; InAs/GaSb/AlSb T2SL; AlAs<sub>0.1</sub>Sb<sub>0.9</sub>/GaSb barrier; bulk detectivity



Preprints.org is a free multidisciplinary platform providing preprint service that is dedicated to making early versions of research outputs permanently available and citable. Preprints posted at Preprints.org appear in Web of Science, Crossref, Google Scholar, Scilit, Europe PMC.

Copyright: This open access article is published under a Creative Commons CC BY 4.0 license, which permit the free download, distribution, and reuse, provided that the author and preprint are cited in any reuse.

## Article

# Extended Short-Wave Infrared T2SL Detector Based on AlAsSb/GaSb Barrier Optimization

Jing Yu <sup>1,2</sup>, Yuegang Fu <sup>1</sup>, Lidan Lu <sup>2</sup>, Weiqiang Chen <sup>2</sup>, Jianzhen Ou <sup>3,\*</sup> and Lianqing Zhu <sup>2,\*</sup>

<sup>1</sup> Changchun University of Science and Technology The School of Electro-Optical Engineering, Changchun 130022, China; 2021200061@mails.cust.edu.cn (J.Y.); fuyg@cust.edu.cn (Y.F.);

<sup>2</sup> School of Instrument Science and Opto-Electronics Engineering, Beijing Information Science and Technology University, Beijing 100192, China; lldan\_dido@bistu.edu.cn (L.L.); 18363996991@163.com (W.C.);

<sup>3</sup> School of Engineering, RMIT University, Melbourne 3000, Australia; jianzhen.ou@rmit.edu.au (J.O.)

\* Correspondence: jianzhen.ou@rmit.edu.au (J.O.); zhulianqing2020@126.com (L.Z.);

**Abstract:** Extended short-wave infrared (eSWIR) detectors operating at high temperatures are widely utilized in planetary science. A high-performance eSWIR based on pBin InAs/GaSb/AlSb type-II superlattice (T2SL) grown on a GaSb substrate was demonstrated. It achieves the optimization of the device's optoelectronic performance by adjusting the p-type doping concentration in the AlAs<sub>0.1</sub>Sb<sub>0.9</sub>/GaSb barrier. Experimental and TCAD simulation results demonstrate that both the device's dark current and responsivity grow as the doping concentration rise. Here, the bulk dark current density and bulk differential resistance area was extracted to calculate the bulk detectivity for evaluating the photoelectric performance of the device. When the barrier concentration is  $1 \times 10^{17} \text{ cm}^{-3}$ , the bulk detectivity is  $2.1 \times 10^{11} \text{ cm} \cdot \text{Hz}^{1/2}/\text{W}$ , which is 256% higher than the concentration of  $2 \times 10^{18} \text{ cm}^{-3}$ . Moreover, at 300K (-10 mV), the 100% cutoff wavelength of the device is  $1.9 \mu\text{m}$ , the dark current density is  $9.48 \times 10^{-6} \text{ A/cm}^2$ , and the peak specific detectivity is  $7.59 \times 10^{10} \text{ cm} \cdot \text{Hz}^{1/2}/\text{W}$  (at  $1.6 \mu\text{m}$ ). The eSWIR detectors with low operating bias and low dark current density hold promise for being developed into high-performance imagers.

**Keywords:** eSWIR; InAs/GaSb/AlSb T2SL; AlAs<sub>0.1</sub>Sb<sub>0.9</sub>/GaSb barrier; bulk detectivity

## 1. Introduction

Compared with traditional shortwave infrared, the extended shortwave infrared (eSWIR) detector ( $1.7 \mu\text{m}$ - $2.5 \mu\text{m}$ ) has a significant advantage in terms of image quality 1. In a degraded visual environment (smoke, haze, or specific dust), the eSWIR detector can capture targets at a longer distance 2. It is widely used in military, earth sciences, satellite remote sensing, and optical communication systems 3. In addition, the eSWIR spectral imaging capability can also be utilized by NASA for planetary science, primarily to study the Earth's surface as well as other nearby celestial bodies 4.

To better serve the application fields of eSWIR, a multitude of material systems have been studied. InGaAs based on InP substrate lattice matching is commonly used for  $1.7 \mu\text{m}$  detection. In order to expand the detection wavelength, InGaAs need to increase the In component, which leads to lattice mismatch. Therefore, the defects of the material will cause serious degradation of the device performance 5. HgCdTe material has good wavelength tunability and can cover the eSWIR spectral region. However, the difficulty of growing HgCdTe materials (inhomogeneity and low yield), the high cost of the CdZnTe substrate, and the complex device manufacturing process make this solution insufficient for an inexpensive eSWIR detector 6. Type-II superlattice (T2SL) materials have the advantages of strong band-gap adjustment flexibility, high carrier effective mass, and good growth uniformity in large areas 7. InGaAs/GaAsSb T2SL structures can achieve a narrower band gap than

InGaAs or GaAsSb. Its lattice-matching growth on the InP substrate can greatly reduce the dislocation in epitaxy 8. R.Sidhu et al. have successfully extended the wavelength of InGaAs/GaAsSb to 2.4  $\mu\text{m}$  9, and researchers are still trying to expand the wavelength. The M structure based on the InAs/GaSb/AlSb material system has greater carrier effective mass and greater band gap tuning freedom 10. A p-i-n homogeneous focal plane array imager based on InAs/GaSb/AlSb has been proved 1.

In order to improve the performance of the device, it is necessary to suppress the dark current density to enhance the specific detectivity and responsivity of the photodetector. The characteristic of nBn architecture is that its unique electronic barrier is designed to block the dark current without hindering the photocurrent 11. Arash Dehzangi et al. combined the large bandgap electron barrier  $\text{AlAs}_{0.1}\text{Sb}_{0.9}/\text{GaSb}$  with InAs/GaSb/AlSb nBn structure to realize an eSWIR detector with low dark current density 12. PBn structure can also create a unipolar barrier, which can successfully block the dark current related to the depletion region. It also has the advantage of very low voltage bias dependence. Jiang et al. adopted the PBn structure to suppress the dark current of the device and improve the quantum efficiency 13. Besides, the pBin structure can also extend the device's absorption into the visible light spectrum. It utilizes large bandgap  $\text{AlAs}_{0.1}\text{Sb}_{0.9}/\text{GaSb}$  materials as window layers and designs the band alignment of this heterointerface to effectively extract photogenerated carriers. Arash Dehzangi et al. demonstrated a visible/extended shortwave infrared detector based on the InAs/AlSb/GaSb T2SL 14. However, the effect of large band gap  $\text{AlAs}_{0.1}\text{Sb}_{0.9}/\text{GaSb}$  materials on the photoelectric performance of InAs/GaSb/AlSb T2SL eSWIR devices still lacks detailed investigation.

This paper presents an InAs/GaSb/AlSb/GaSb T2SL eSWIR detector based on a pBin structure with a 100% cutoff wavelength of 1.9  $\mu\text{m}$ . By optimizing the doping concentration of the  $\text{AlAs}_{0.1}\text{Sb}_{0.9}/\text{GaSb}$  barrier, the device achieves high performance specific detectivity. The experimental results are consistent with the simulation results. With the increase of the doping concentration of the barrier structure, the dark current and the responsivity of the device also increase. By separating the bulk dark current and surface dark current of the device, we determined that the optimal doping concentration of the barrier is p-type  $1 \times 10^{17} \text{ cm}^{-3}$ . The bulk detectivity of the device is maximized to  $2.1 \times 10^{11} \text{ cm} \cdot \text{Hz}^{1/2}/\text{W}$ .

## 2. Design, Growth, and Fabrication

The material was grown on an n-type GaSb (001) substrate by molecular beam epitaxy (MBE) system of Komponenten, Germany. As shown in Figure 1a, it is the designed pBin type eSWIR device structure. Firstly, a 500 nm GaSb buffer layer (p-type  $2 \times 10^{18} \text{ cm}^{-3}$ ) was epitaxially grown on the GaSb substrate. Then, the bottom contact layer is 500 nm 6/1/5/1 mono-layers (MLs) of InAs/GaSb/AlSb/GaSb (p-type  $10^{18} \text{ cm}^{-3}$ ). The second electron barrier layer is 150 nm 5/2 MLs of  $\text{AlAs}_{0.1}\text{Sb}_{0.9}/\text{GaSb}$ . Due to the difference in the valence band position between the barrier and the absorption region material, the valence band position of the barrier is adjusted by intentional doping. During the experiment, different beryllium (Be) doping source temperatures were used to achieve precise control of the material doping concentration. The doping concentration values corresponding to the temperature of the Be source are precisely calibrated by means of the Hall test. The doping concentrations of Z1, Z2, and Z3 were  $1 \times 10^{15} \text{ cm}^{-3}$ ,  $1 \times 10^{17} \text{ cm}^{-3}$ , and  $2 \times 10^{18} \text{ cm}^{-3}$ , respectively. Subsequently, the first electron barrier layer is 100 nm 4/1/5/1 MLs of InAs/GaSb/AlSb/GaSb (undoped, n-type  $10^{14} \text{ cm}^{-3}$ ). The absorption region is 1000 nm 6/1/5/1 MLs of InAs/GaSb/AlSb/GaSb (undoped, n-type  $10^{14} \text{ cm}^{-3}$ ) T2SL material. The top contact layer is 200 nm 6/1/5/1 MLs of InAs/GaSb/AlSb/GaSb (n-type  $2 \times 10^{18} \text{ cm}^{-3}$ ), and the last 30 nm InAs (n-type  $10^{19} \text{ cm}^{-3}$ ) serves as the cap layer of the device. Figure 1b,c are high-resolution X-ray diffraction (HRXRD) and atomic force microscopy (AFM) images of sample Z2, respectively. The HRXRD satellite peak results show that the periodic thicknesses of the absorption region, first barrier region, and second barrier region are approximately 3.85nm, 3.37nm, and 2.07nm, respectively. The stress mismatch between the above superlattice materials and GaSb is within 0.1%, which is consistent with the superlattice design. AFM

displays clear atomic steps on the surface of the material, with a Root Mean Square (RMS) roughness of only 0.125nm in the 5×5  $\mu\text{m}^2$  region. The surface quality of the material is high. Samples Z1 and Z3 have similar lattice quality and surface quality.

The three devices were prepared using the same batch device manufacturing process. The circular mesa was wet-etched with  $\text{C}_6\text{H}_8\text{O}_7:\text{H}_3\text{PO}_4:\text{H}_2\text{O}_2:\text{H}_2\text{O}$  (5 g:2 mL:1 mL:20 mL) solution. The solution has an etching rate of about 150 nm/min and can precisely control the etching depth to the p-type bottom contact layer. These devices have not been passivated. Finally, Ti/Au (10 nm/100 nm) was deposited on the InAs cap layer (n-type) and bottom contact (p-type) using electron beam evaporation for metallization.

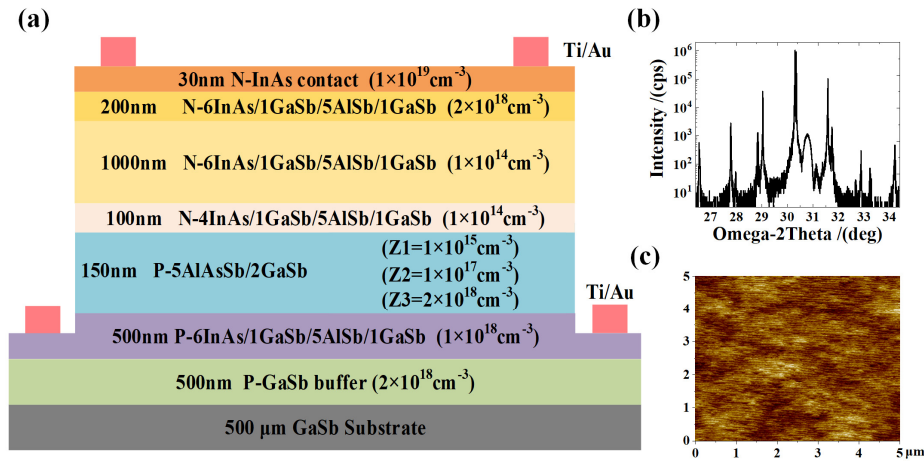


**Figure 1.** (a) Structure diagram of pBin eSWIR photodetector with Ti/Au metal contact layer; (b) HRXRD results of sample Z2; (c) The RMS roughness of AFM image is 0.125 nm in 5×5  $\mu\text{m}^2$  area.

### 3. Results and Discussion

#### 3.1. Experimental Result

To verify the electrical performance of different devices at 300K, the current and voltage characteristics of devices Z1, Z2, and Z3 were measured. The experiment used a semiconductor analyzer (B1500A) as the voltage source and applied a bias voltage to the device through the probe arm of a low-temperature probe station (CRX-VF). The total dark current of the device includes bulk dark current and surface dark current. In order to investigate the effect of  $\text{AlAs}_{0.1}\text{Sb}_{0.9}/\text{GaSb}$  barrier on the dark currents of devices Z1, Z2, and Z3, it is necessary to separate the surface dark currents of devices. Therefore, the current-voltage characteristic curves of devices with different sizes are tested. The bulk current density ( $J_b$ ) and surface dark current density ( $J_s$ ) of the device can be separated by the following Equation (15):

$$J_D = J_b + J_s \cdot (P/A) \quad (1)$$

where  $J_D$  is the total dark current density of the device,  $P$  is the mesa perimeter, and  $A$  is the mesa area of the device. As shown in Figure 2a, the  $J_D$  (at -10 mV) of devices Z1, Z2, and Z3 were extracted. The  $J_D$  of device Z1 is the smallest and the  $J_D$  of device Z3 is the largest. Subsequently, Equation (1) was used to fit the  $J_D$  of different devices. The fitting results show that the  $J_d$  of the devices Z1, Z2, and Z3 are  $1.06 \times 10^{-6} \text{ A/cm}^2$ ,  $1.17 \times 10^{-6} \text{ A/cm}^2$ , and  $1.875 \times 10^{-5} \text{ A/cm}^2$ , respectively. Besides,  $J_D$  is also showing an increasing trend. The bulk differential resistance area  $(R_A)_b$  of the device is separated in the same way for the bulk detectivity calculation of the device. The fit uses the following Equation (16):

$$\frac{1}{R_A} = \frac{1}{(R_A)_b} + \frac{1}{r_s} \frac{P}{A} \quad (2)$$



where  $R_A$  is the total differential resistance area of the device and  $r_s$  is the surface resistivity of the device. The fitting results showed that the  $1/(R_A)_b$  of the devices Z1, Z2, and Z3 were  $9.62 \times 10^{-5} \Omega^{-1} \cdot \text{cm}^{-2}$ ,  $1.03 \times 10^{-4} \Omega^{-1} \cdot \text{cm}^{-2}$ , and  $1.58 \times 10^{-3} \Omega^{-1} \cdot \text{cm}^{-2}$ , respectively. The  $(R_A)_b$  of the device shows a decreasing trend as the doping concentration of the  $\text{AlAs}_{0.1}\text{Sb}_{0.9}/\text{GaSb}$  barrier increases.

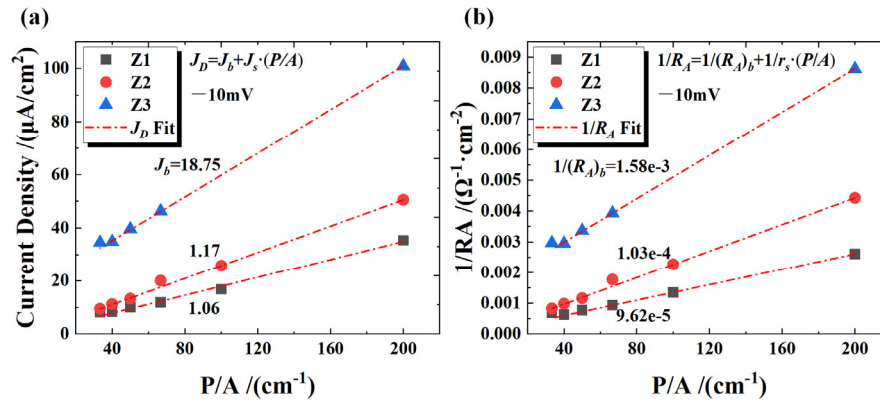


**Figure 2.** (a) The dark current density for different device sizes is fitted; (b) The differential resistance area for different device sizes is fitted.

To verify whether there are differences in the optical properties of different devices under the condition of 300K, we conducted spectral response tests on devices Z1, Z2, and Z3. Fourier transform infrared (FTIR) spectrometer (Bruker FTIR VERTEX 80/80v) was used to measure the spectral response of the device. By setting the sensitivity of the current amplifier (SR570) to  $200 \mu\text{A}/\text{V}$ , the optical signal received by the device is amplified, and then the spectral information is obtained through the digital-to-analog converter. Finally, the device responsivity is measured using a calibrated 1273K blackbody source. As shown in Figure 3a, the responsivity of the devices Z1, Z2, and Z3 at a wavelength of  $1.55 \mu\text{m}$  is  $0.26 \text{ A}/\text{W}$ ,  $0.30 \text{ A}/\text{W}$ , and  $0.33 \text{ A}/\text{W}$ , respectively. Furthermore, the spectral response test results show that the 100% cutoff wavelength of all three devices is about  $1.9 \mu\text{m}$ . Then, the spectral response curves are normalized by using the responsivity at  $1.55 \mu\text{m}$  to obtain the responsivity across the full wavelength range (Figure 3c). Therefore, the device responsivity increases with the increase of  $\text{AlAs}_{0.1}\text{Sb}_{0.9}/\text{GaSb}$  doping concentration. This phenomenon shows the same variation trend as the  $J_d$  of the device. Although the device Z3 has a high responsivity, it also has a large  $J_d$ . To further evaluate the comprehensive performance of devices Z1, Z2, and Z3, we neglected the  $J_s$  component of the devices and calculated their bulk detectivity  $D_b^*$  using  $J_d$  and  $(R_A)_b$ . The calculation formula is as follows:

$$D_b^* = \frac{R_i}{\sqrt{2qJ_b + \frac{4k_B T}{(R_A)_b}}} \quad (3)$$

where  $R_i$  is the device responsivity,  $q$  is the fundamental charge,  $k_B$  is the Boltzmann constant, and  $T$  is the device operating temperature (at 300K). Figure 3b shows that the  $D_b^*$  of devices Z1, Z2, and Z3 are  $1.8 \times 10^{11} \text{ cm} \cdot \text{Hz}^{1/2}/\text{W}$ ,  $2.1 \times 10^{11} \text{ cm} \cdot \text{Hz}^{1/2}/\text{W}$ , and  $5.9 \times 10^{10} \text{ cm} \cdot \text{Hz}^{1/2}/\text{W}$ , respectively. The  $D_b^*$  of the device shows a trend of first increasing and then decreasing. Device Z2 exhibits the best comprehensive performance and has an improvement of 256% compared to device Z3. In addition, we also calculated the specific detectivity  $D^* = R_i (2qJ_b + 4k_B T / R_A)^{-1/2}$  of devices Z1, Z2, and Z3 (with a diameter of  $1200 \mu\text{m}$ ) under full spectrum. As shown in Figure 3d, device Z2 has the highest specific detectivity (its dark current density is  $9.48 \times 10^{-6} \text{ A}/\text{cm}^2$  at a bias of  $-10 \text{ mV}$ ), and the peak specific detectivity is  $7.59 \times 10^{10} \text{ cm} \cdot \text{Hz}^{1/2}/\text{W}$  at  $1.6 \mu\text{m}$ . Device Z2 has improved by approximately 73% compared to device Z3. Table 1 shows the performance comparison between device Z2 and other

eSWIR detectors. The specific detectivity of our device has certain advantages compared to other detectors.

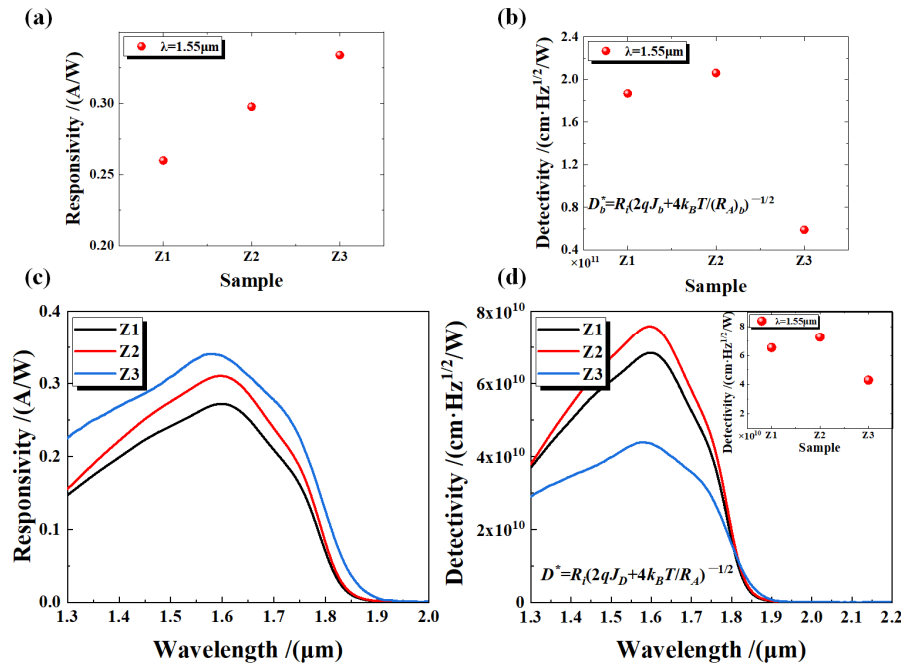


**Figure 3.** (a) The responsivity of devices Z1, Z2, and Z3 under blackbody testing; (b) The values of the bulk detectivity of the device without  $J_s$  at 1.55 μm; (c) The normalized responsivity of devices Z1, Z2, and Z3 under a -10 mV bias; (d) The spectral specific detectivity of these devices with a diameter of 1200 μm.

**Table 1.** The performance of eSWIR photodetectors is compared with other eSWIR photodetectors.

	Temperature (K)	Cutoff Wavelength (μm)	Specific Detectivity (cm·Hz <sup>1/2</sup> /W)
Ref. 4	300	2.4	4.72×10 <sup>10</sup> (-20mV)
Ref. 13	300	2.2	2.5×10 <sup>10</sup> (-10mV)
Ref. 19	300	2.3	8.18×10 <sup>9</sup> (-20mV)
This paper	300	1.9	7.59×10 <sup>10</sup> (-10mV)

### 3.2. Simulation and Discussion

Aiming at the problem that the doping concentration of AlAs<sub>0.1</sub>Sb<sub>0.9</sub>/GaSb changes the current of the device, we use simulation tools to further explain the experimental results. In this study, the performance of semiconductor devices was numerically simulated using Technology Computer Aided Design (TCAD) models 20, including mobility models (parallel electric field-dependent model), recombination models (Shockley-Read-Hall recombination model, Auger recombination model, and optical recombination model), and carrier statistics models (Fermi-Dirac statistics model). The properties of superlattice materials were calculated by weighted average of InAs, GaSb, AlSb and AlAs compounds 21. These include conduction band density ( $N_c$ ), valence band density ( $N_v$ ), electron mobility ( $\mu_n$ ), hole mobility ( $\mu_p$ ), and dielectric constant. Moreover, the bandgap energy of superlattice materials is calculated using the 8kp model 22. Table 2 shows the partial parameter values (at 300K) of 6/1/5/1 MLs of InAs/GaSb/AlSb/GaSb, 4/1/5/1 MLs of InAs/GaSb/AlSb/GaSb, and 5/2 MLs of AlAs<sub>0.1</sub>Sb<sub>0.9</sub>/GaSb superlattice materials. The model was solved by Newton and Gummel combinatorial iterative method.

**Table 2.** Some material parameters are used for TCAD model simulation.

Material	Bandgap/eV	$N_d/\text{cm}^{-3}$	$N_v/\text{cm}^{-3}$	$\mu_n/\text{cm}^2/\text{V}\cdot\text{s}$	$\mu_p/\text{cm}^2/\text{V}\cdot\text{s}$	dielectric constant
6InAs/1GaSb/5AlSb/1GaSb	0.65	$1.4 \times 10^{17}$	$9.1 \times 10^{18}$	27717	702	13.4
4InAs/1GaSb/5AlSb/1GaSb	0.75	$1.7 \times 10^{17}$	$1.1 \times 10^{19}$	20219	772	12.4
5AlAs <sub>0.1</sub> Sb <sub>0.9</sub> /2GaSb	1.25	$8.2 \times 10^{16}$	$6.7 \times 10^{18}$	2720	914	15.4

We simulated the effects of AlAs<sub>0.1</sub>Sb<sub>0.9</sub>/GaSb with varying doping concentrations on the optoelectronic performance of the devices. The InAs material at the top of the device is taken as the origin, and the opposite direction of material epitaxy is taken as the positive direction to establish the coordinate system. The conduction and valence bands of the material (at -10 mV) are shown in Figure 4a. This includes a 30 nm InAs cap layer (n-type  $1 \times 10^{19} \text{ cm}^{-3}$ ), a 200 nm top contact layer (n-type  $2 \times 10^{18} \text{ cm}^{-3}$ ) serving as a photogenerated hole carrier extractor, a 1000 nm absorption region (unintentionally doped, n-type  $1 \times 10^{14} \text{ cm}^{-3}$ ) for generating photogenerated carriers, a 100 nm first electron barrier region (unintentionally doped, n-type  $1 \times 10^{14} \text{ cm}^{-3}$ ), a 150 nm second electron barrier region (p-type:  $P_1 = 1 \times 10^{15} \text{ cm}^{-3}$ ,  $P_2 = 1 \times 10^{17} \text{ cm}^{-3}$ ,  $P_3 = 2 \times 10^{18} \text{ cm}^{-3}$ ), and a 500 nm bottom contact layer (p-type  $1 \times 10^{18} \text{ cm}^{-3}$ ) acting as a photogenerated electron extractor.

Figure 4a shows that the first and second electron barriers with a wide band gap in the device structure can reduce the partial generation-recombination dark current. The second electron barrier can also block the passage of thermally excited electrons [4]. The valence band maximum energy  $E_v$  and the conduction band minimum energy  $E_c$  both shift up as the doping concentration of AlAs<sub>0.1</sub>Sb<sub>0.9</sub>/GaSb increases. Figure 4b shows the simulation data of dark current under different bias voltages. The results indicate that the dark current of the device increases with the rising p-type doping concentration in AlAs<sub>0.1</sub>Sb<sub>0.9</sub>/GaSb. This may be caused by the high hole concentration of AlAs<sub>0.1</sub>Sb<sub>0.9</sub>/GaSb. Under thermal excitation, holes pass through the first electron barrier region to reach the top contact layer, resulting in a larger dark current. Besides, at the illumination of  $1.55 \mu\text{m}$ , we can simulate the photocurrent data in Figure 4c. Under -10 mV bias, the photocurrent increases with the increase of AlAs<sub>0.1</sub>Sb<sub>0.9</sub>/GaSb doping concentration. In the absorption region, photogenerated carriers (holes and electrons) are generated under optical excitation, with the top contact layer extracting electrons and the bottom contact layer extracting holes. Due to the upward shift of the  $E_v$  in the AlAs<sub>0.1</sub>Sb<sub>0.9</sub>/GaSb barrier, the photocurrent increases as the bottom contact layer extracts more photogenerated hole carriers. Therefore, the simulation data demonstrate that the variation trends of photocurrent and dark current align with the experimental data.

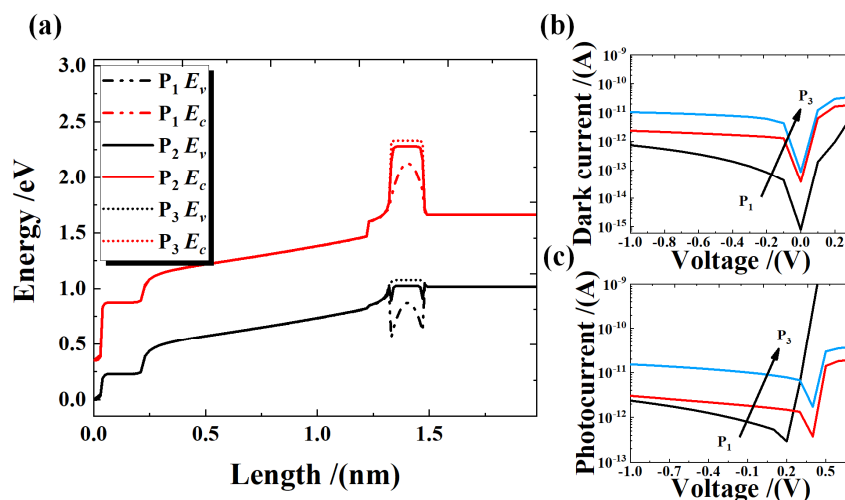


**Figure 4.** (a) The  $E_c$  and  $E_v$  diagram of the material; The variation trends of dark current (b) and photocurrent (c) under different doping concentrations in the AlAs<sub>0.1</sub>Sb<sub>0.9</sub>/GaSb barrier region.

## 4. Conclusion

In summary, an InAs/GaSb/AlSb T2SL photodetector based on the optimization of the  $\text{AlAs}_{0.1}\text{Sb}_{0.9}/\text{GaSb}$  barrier has been designed. Both experimental and simulated studies employed device structures with three different p-type doping concentrations in the  $\text{AlAs}_{0.1}\text{Sb}_{0.9}/\text{GaSb}$  barrier. The results consistently demonstrate that the current increases with elevated p-type doping concentrations in the barrier. Therefore, we evaluated the device performance by comparing bulk detectivity  $D_b^*$ . The optimized eSWIR detector achieved a peak specific detectivity  $D^*$  of  $7.59 \times 10^{10} \text{ cm} \cdot \text{Hz}^{1/2}/\text{W}$  at  $1.6 \mu\text{m}$ , representing a ~73% improvement. Additionally, the detector exhibits a 100% cutoff wavelength of  $1.9 \mu\text{m}$  at 300 K, with a dark current density of  $9.48 \times 10^{-6} \text{ A/cm}^2$  under a -10 mV bias. This work provides a design strategy for advanced eSWIR device architectures and enables the fabrication of high-performance eSWIR imagers.

**Author Contributions:** Conceptualization, L.Z., L.L., Y.F. and J.O.; methodology, J.Y.; software, W.C.; validation, J.Y., L.L. and W.C.; formal analysis, L.Z., Y.F. and J.O.; investigation, L.L.; resources, L.Z., Y.F. and J.O.; data curation, J.Y.; writing—original draft preparation, J.Y.; writing—review and editing, J.Y., L.L., and W.C. All authors have read and agreed to the published version of the manuscript.

**Funding:** This research was funded by the National Key Research and Development Sub project (2022YFF0705801); National Natural Science Foundation of China (62205029); Young Elite Scientists Sponsorship Program by CAST (2022QNR001).

**Data Availability Statement:** The data supporting this study's findings are available within the article.

**Conflicts of Interest:** The authors declare no conflict of interest.

## References

1. Hoang, A. M.; Chen, G.; Haddadi, A.; Abdollahi Pour, S.; Razeghi, M., Demonstration of shortwavelength infrared photodiodes based on type-II InAs/GaSb/AlSb superlattices. *Applied Physics Letters*, 2012, 100 (21), 211101. <https://doi.org/10.1063/1.4720094>.
2. Lindsey, W.; Joshua, F.; Patrick, L.; Orges, F.; Rich, P.; David, B.; Ronald, D. In *Target discrimination in the extended SWIR (eSWIR) band (2-2.5 μm) compared to Vis, NIR, and SWIR in degraded visual environments*, Proc.SPIE, 2022; p 1210606. 41-51. <https://doi.org/10.1117/12.2618566>.
3. Gao, B.-c., NDWI—A normalized difference water index for remote sensing of vegetation liquid water from space. *Remote Sensing of Environment* **1996**, 58 (3), 257-266. [https://doi.org/10.1016/S0034-4257\(96\)00067-3](https://doi.org/10.1016/S0034-4257(96)00067-3).
4. Dehzangi, A.; McClintock, R.; Haddadi, A.; Wu, D.; Chevallier, R.; Razeghi, M., Type-II superlattices base visible/extended short-wavelength infrared photodetectors with a bandstructure-engineered photo-generated carrier extractor. *Scientific Reports*, **2019**, 9 (1), 5003. <https://doi.org/10.1038/s41598-019-41494-6>.
5. Arslan, Y.; Oguz, F.; Besikci, C., Extended wavelength SWIR InGaAs focal plane array: Characteristics and limitations. *Infrared Physics & Technology*, **2015**, 70, 134-137. <https://doi.org/10.1016/j.infrared.2014.10.012>.
6. Tennant, W. E.; Cockrum, C. A.; Gilpin, J. B.; Kinch, M. A.; Reine, M. B.; Ruth, R. P., Key issues in HgCdTe-based focal plane arrays: An industry perspective. *Journal of Vacuum Science & Technology B: Microelectronics and Nanometer Structures Processing, Measurement, and Phenomena*, **1992**, 10 (4), 1359-1369. <https://doi.org/10.1116/1.585869>.
7. Piquini, P.; Zunger, A.; Magri, R., Pseudopotential calculations of band gaps and band edges of short-period  $(\text{InAs})_n/(\text{GaSb})_m$  superlattices with different substrates, layer orientations, and interfacial bonds. *Physical Review B*, **2008**, 77 (11), 115314. DOI: <https://doi.org/10.1103/PhysRevB.77.115314>.
8. Easley, J.; Martin, C. R.; Ettenberg, M. H.; Phillips, J., InGaAs/GaAsSb Type-II Superlattices for Short-Wavelength Infrared Detection. *Journal of Electronic Materials*, **2019**, 48 (10), 6025-6029, doi:10.1007/s11664-019-07441-x.
9. Sidhu, R.; Ning, D.; Campbell, J. C.; Holmes, A. L., A long-wavelength photodiode on InP using lattice-matched GaInAs-GaAsSb type-II quantum wells. *IEEE Photonics Technology Letters*, **2005**, 17 (12), 2715-2717. doi:10.1109/LPT.2005.859163.



10. Nguyen, B. M.; Razeghi, M.; Nathan, V.; Gail, J. B. In *Type-II M structure photodiodes: an alternative material design for mid-wave to long wavelength infrared regimes*, Proc. SPIE, 2007, 6479, 113-122. <https://doi.org/10.1117/12.711588>.
11. Nguyen, B.-M.; Hoffman, D.; Delaunay, P.-Y.; Razeghi, M., Dark current suppression in type II InAs / GaSb superlattice long wavelength infrared photodiodes with M-structure barrier. *Applied Physics Letters*, **2007**, 91 (16), 163511. <https://doi.org/10.1063/1.2800808>.
12. Dehzangi, A.; Haddadi, A.; Chevallier, R.; Zhang, Y.; Razeghi, M., nBn extended short-wavelength infrared focal plane array. *Opt. Lett.*, **2018**, 43 (3), 591-594. <https://doi.org/10.1364/OL.43.000591>.
13. Jiang, J.; Chang, F.; Zhou, W.; Li, N.; Chen, W.; Jiang, D.; Hao, H.; Wang, G.; Wu, D.; Xu, Y.; Niu, Z.-C., High-performance extended short-wavelength infrared Pbn photodetectors based on InAs/GaSb/AlSb superlattices. *Chinese Physics B*, **2023**, 32 (3), 038503. DOI 10.1088/1674-1056/acaa2e.
14. Dehzangi, A.; Haddadi, A.; Chevallier, R.; Zhang, Y.; Razeghi, M., Fabrication of 12  $\mu\text{m}$  pixel-pitch 1280  $\times$  1024 extended short wavelength infrared focal plane array using heterojunction type-II superlattice-based photodetectors. *Semiconductor Science and Technology*, **2019**, 34 (3), 03LT01. DOI 10.1088/1361-6641/aaf770.
15. Campbell, J. C., Recent Advances in Avalanche Photodiodes. *Journal of Lightwave Technology*, **2016**, 34 (2), 278-285. DOI: 10.1109/JLT.2015.2453092.
16. Li, H.; Lu, L.; Yu, J.; Zheng, X.; Zhang, D.; Chen, W.; Feng, Y.; Ren, G.; Zhu, L., Low dark current density extended short-wavelength infrared superlattice photodetector with atomic layer deposited Al<sub>2</sub>O<sub>3</sub> passivation. *Appl. Opt.*, **2023**, 62 (30), 7960-7965. <https://doi.org/10.1364/AO.501175>.
17. Li, N.; Sun, J.; Jia, Q.; Song, Y.; Jiang, D.; Wang, G.; Xu, Y.; Niu, Z., High performance nBn detectors based on InGaAsSb bulk materials for short wavelength infrared detection. *AIP Advances*, **2019**, 9 (10), 105106. doi:10.1063/1.5124093.
18. Mark, D. N.; Jerris, F. J.; Terrence, S. L., General noise processes in hybrid infrared focal plane arrays. *Optical Engineering*, **1991**, 30 (11), 1682-1700. doi:doi.org/10.1117/12.55996.
19. Xie, R.; Shan, Y.; Liang, Y.; Yao, L.; Su, X.; Wu, D.; Hao, H.; Jiang, D.; Wang, G.; Xu, Y.; Ni, H.; Niu, Z., Extended Short-Wave Infrared Barrier Structure Focal Plane Array Based on InGaAs/GaAsSb Type-II Superlattices. *Journal of Lightwave Technology* **2024**, 1-6. DOI: 10.1109/JLT.2024.3491901.
20. Maiti, C. K., *Introducing Technology Computer-Aided Design (TCAD): Fundamentals, Simulations, and Applications*. Jenny Stanford Publishing: 2017. <https://doi.org/10.1201/9781315364506>.
21. A. Jones. Al<sub>x</sub>In<sub>1-x</sub>As<sub>y</sub>Sb<sub>1-y</sub> Digital Alloy Avalanche Photodiodes for Low-Noise Applications. University of Virginia, 2020. doi: 10.18130/V3-X75T-MS29.
22. Yu, J.; Zhu, L.; Lu, L.; Chen, W.; Zheng, X.; Zhang, D.; Fu, Y.; Ou, J. Interface Engineering and Electron-Hole Wave Function Overlap of InAs/AlSb Superlattice Infrared Detectors. *Photonics*, **2023**, 10 (11), 1268. <https://doi.org/10.3390/photonics10111268>.

**Disclaimer/Publisher's Note:** The statements, opinions and data contained in all publications are solely those of the individual author(s) and contributor(s) and not of MDPI and/or the editor(s). MDPI and/or the editor(s) disclaim responsibility for any injury to people or property resulting from any ideas, methods, instructions or products referred to in the content.